Int J Adv Manuf Technol (2016) 84:1801–1820
DOI 10.1007/s00170-015-7826-3

ORIGINAL ARTICLE

Cutting forces and their modelling in plunge milling of magnesium-rare earth alloys

Isabelle Danis[1] · Frédéric Monies[1] · Pierre Lagarrigue[1] · Nathalie Wojtowicz[1]

Received: 8 June 2015 / Accepted: 8 September 2015 / Published online: 21 September 2015

Abstract Plunge milling is a machining process already recognised as able to afford significant gains in productivity during the roughing phases, especially in the case of deep workpieces. It is generally used for machining hard materials but more rarely for light alloys, especially for magnesium alloys. This paper deals with the study and the modeling of cutting forces in plunge milling of magnesium-rare earth alloys. In this study, the authors consider the case of a dry plunge milling process applied to two wrought Mg-Zr-Zn-RE alloys and one cast Mg-Zr-Zn-RE alloy, that are representative of magnesium-rare earth alloys in aerospace industry. This paper investigates the influence of cutting parameters and the influence of edge radius on cutting forces. An analytical model is set up so as to satisfactorily predict the cutting forces for these three representative magnesium alloys studied using just three instrumented tests. An experimental validation through different plunge milling tests shows good agreement between the model and the measured values in a wide range of cutting conditions.

Keywords Plunge milling · Cutting forces · Modelling · Mg-Zr-Zn-RE alloys

1 Introduction

Plunge milling is a roughing process used to remove material. It allows major gains in productivity especially in deep workpieces (casings). It involves a series of successive plunges into the stock, each time separated by a radial offset value noted ae (Figs. 1 and 2). The cutter then only works axially. For lateral plunge milling, the cutter moves between each plunge parallel to the wall to be produced. When full width cut plunge milling, the cutter is fully engaged in the material, the cutting width being equal to the cutter diameter (Figs. 1 and 2). The fact that the cutter moves a certain distance before again plunging into the material means that characteristic scallops are left, as visible on Fig. 1. The height of these scallops h (Fig. 2) will depend on the cutter diameter and the radial offset ae, representing a major parameter for the operation's success: indeed, if plunge milling is used for roughing, it is important to plan for a finishing process in order to determine what scallop height h can be left; if plunge milling is used in finishing, this value h must respect the workpiece's shape tolerances.

On each plunge in full-slot milling, the cutter will remove a crescent shaped volume of material as shown in red on Fig. 2 on the height of the pocket to be machined. The area of the crescent is expressed as follows:

$$A_{\text{crescent}} = 2R^2\,|\theta_e| + ae.R\cos\theta_e \tag{1}$$

with :

$$\theta_e = \arcsin\left(\frac{ae}{2R}\right) \tag{2}$$

where R is the cutter radius, and θ_e is the cutter's angle of entry into the material (Fig. 2).

A large number of studies has been already lead in milling, focusing on cutting forces and their modelling [1–5]. Since few years, specific studies on plunge milling can be found. The main advantage of plunge milling as vaunted by cutting tool manufacturers lies in the gains in productivity it has to offer and the preponderance of axial forces as opposed to lateral forces, which automatically

✉ Frédéric Monies
frederic.monies@univ-tlse3.fr

[1] Université de Toulouse 3, ICA (Institut Clément Ader), 118, route de Narbonne, F-31062, Toulouse, France

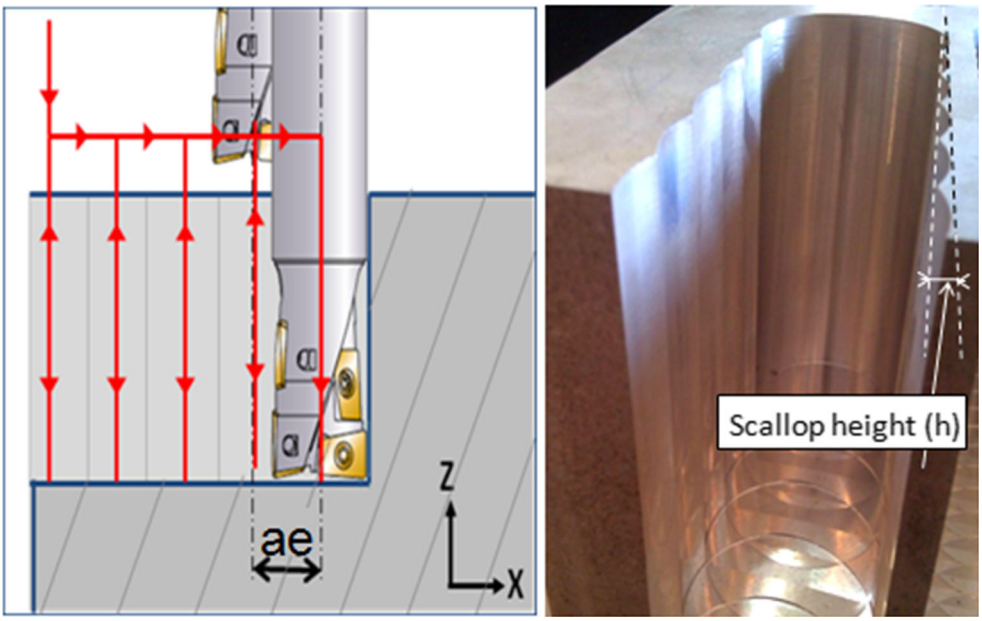

Fig. 1 Full width cut plunge milling

implies extremely good cutting stability. Now, the first thing to be noted when reviewing the various studies on plunge milling published in the literature is that such a claim is not always verified. While Altintas and Ko see the axial force as being higher than the other forces in continuous plunge milling (drilling or hole widening) [6, 7], other authors observe that the axial force is not the preponderant force [8–12]. However, nearly all authors agree that the radial force is found to be considerably reduced as compared with conventional milling operations, clearly providing a dynamic advantage in cutting stability. According to Witty, the ratio axial force on radial force (Fa/Fr) can be modified by playing on the radial offset and on the feed rate for the same tool nose radius, with the most advantageous ratio obviously being the highest possible from a dynamic point of view [8]. However, it is also essential to take the machine-tool's capabilities into account as the spindle bearings can considerably limit the permissible axial forces. The first publication concerning plunge milling was written by Li et al. [11]. He focused on modelling of the cutting forces during an operation allowing complex chamfer shapes to be produced in a hole. This thus involved enlarging an already existing hole. In this study, Li used conventional methods to model milling forces as widely applied and as based on works by Koenigsberger and Sabberwal, or Tlusty and MacNeil: the tangent force is expressed as the product of a specific constant cutting pressure and the instantaneous chip cross-section [13], while the radial force is proportional to the tangent force [14], just like the axial force. The proportionality coefficients are specific cutting pressures representing both the cutter and cutting edge geometries and the properties of the materials involved. The resulting force is then obtained by integration along the different cutting edges. Other studies adopt these same basic principles as with Al-Ahmad [9]. In 2007, Qin used a new and interesting approach for analytical modelling of the cutting forces in plunge milling, considering that this operation can be assimilated with orthogonal cutting [15]. This approach, inspired by turbine blade roughing applications, enabled him to predict the cutting forces by reconstructing the total forces from modelling of the forces relating to each insert. However, only the first plunge into the material is taken into account in this study, where it is not the crescent shown on Fig. 2 that is considered, but a plunge on the edge of the workpiece represented by an arc of a circle limited by a chord. Another type of modelling of cutting forces during plunge milling of vertical walls was proposed by Zhuang in 2012 [16]. The force model is developed in plunge milling of Inconel 718. This modelling is based on the assumption that each force is a power function of the different cutting parameters (feed per tooth, cutting speed and radial offset), where a is the thickness of material taken laterally by the cutter along the wall and ae is the radial offset between each plunge. The various coefficients are then determined experimentally from an experimental design. This study highlights the importance of taking into account both the radial offset between passes and the thickness of the milled wall a. Indeed, the model is closer to the experimental forces when the product $a.ae$ is taken into account, as compared with only considering the thickness of the wall a. Other forms of modelling were proposed by Altintas and Ko, who take the dynamic aspect of the system into account, both in the time domain [7] and the frequency domain [6]. For Ahmed [17], the forces are calculated using mechanistic model as a function of the dynamic chip area cut by each insert. The cutting coefficients are given as a function of the chip thickness, noted w, by the

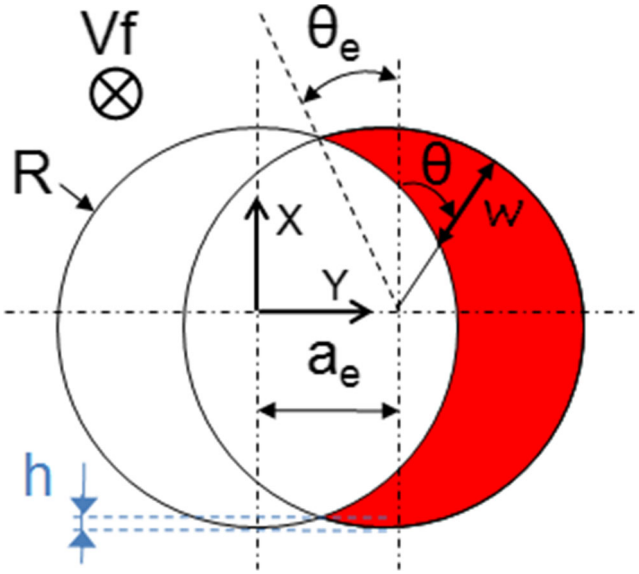

Fig. 2 Chip area for full width cut plunge milling

power function: $K(\mathrm{N/mm^2}) = p.w^{-q}$, where p and q are two coefficients which have to be determined for each coefficients K associated with the tangential force Ft, the radial force Fr and the axial force Fa. In their study, the tests are conducted on a aluminium alloy Al 356.

The authors of the present article are involved in an industrial and academic project, one of whose goals is to reduce manufacturing costs for a machined engine housing made of a magnesium alloy. Reducing costs means increasing chip flow, preferably without any lubrication and especially during roughing operations. This explains why the authors chose to study plunge milling. Magnesium alloys are used because of weights saving: they provide advantages over aluminium, in being of even lower density (approximatively 1800 kg/m^3) than aluminium (about 2800 kg/m^3). The magnesium alloys considered here are Mg-Zr-Zn-RE alloys. They are characterised by low density and good mechanical properties. The rare earth elements have beneficial effect of on the creep properties and thermal stability of structure and mechanical properties of magnesium alloys [18]. They can be used at temperatures up to 200 ∘C and are then well fitted in aeronautical applications. Contrary to its reputation as a highly flammable metal, magnesium is among the industrial metals, the one that best lends itself to machining. The yield can be increased thanks to its intrinsic characteristics. These characteristics allow to shorter machining time, lower tool wear and power requirements in comparison with other metals, especially aluminum alloys. No work has been done, to authors' knowledge, on plunge milling of magnesium alloys, except the work made by Danis et al. [19, 20], where surface integrity was studied. The goal of these studies were to suggest plunge milling conditions to offer a trade-off between surface integrity and chip flow. This paper seeks therefore first to know the cutting forces during plunge milling of these magnesium alloys and the cutting parameters influencing these cutting forces, and then to define a new model adapted to plunge milling and to these new alloys.

First, the methodology and experimental equipments will be presented, as well as the three studied magnesium alloys (forged Elektron 21, forged MRI301F and cast Elektron 21). Second, the cutting forces will be studied for the plunge milling of three alloys. This will allow us to see the force levels achieved, and the parameters influencing these cutting forces (materials, tool geometry). Then, a new cutting force model will be presented, for plunge milling the three magnesium alloys, based on Merchant's orthogonal cutting model, adapted in our case to represent the axial and tangential cutting forces (the radial force is negligible, as it will be demonstrated in this study). A methodology is devised so as to satisfactorily predict the cutting forces over a broad range of cutting conditions from just three instrumented tests.

2 Experimental protocol

The machined materials were Elektron 21 (E21: Mg-Nd-Gd-Zr-Zn), as cast by magnesium elektron (MEL), and MRI301F (Mg-Nd-Y-Zr-Zn), marketed by Dead Sea Magnesium Ltd. The MRI301F and some of the E21 alloy were then forged in France, thus giving three alloys to study: forged E21, forged MRI301F and cast E21. The compositions of the three alloys and their properties are presented in the study conducted by Danis et al. [20]. The Elektron 21 alloy was studied in a few papers [18, 21, 22]. The plunge-milling tests were performed on a DMU 50 eVolution 5-axis NC machine (with a Siemens 840D CNC controller), without lubrication. The test coupons were secured to a Kistler six-component force measurement plate 9257B. The cutting tool used was a 33 mm diameter Mitsubishi AQX milling cutter. Two different types of inserts were used, both designed by Mitsubishi. The HTi10 grade inserts have a polished rake face and a very sharp edge and are designed for the machining of non-ferrous alloys (N alloys). The VP15TF grade inserts are developed to machine most of metals (cast iron, steel, titanium alloys...). This grade is supposed to offer longer tool-life with a good sharpness, despite the PVD coating of (Ti,Al)N which is supposed to avoid welding problems during dry machining. The two types of inserts present the same rake angle of 23° and the same relief angle. The main difference between HTi10 and VP15TF grade inserts for the AQX milling cutter is their sharpness, with an edge radius, noted r_β, of less than 3 µm with the first ones, and about 45 µm for the second ones. The measurements were made first with a scanning electron microscope (SEM). The grade inserts for the AQX cutter

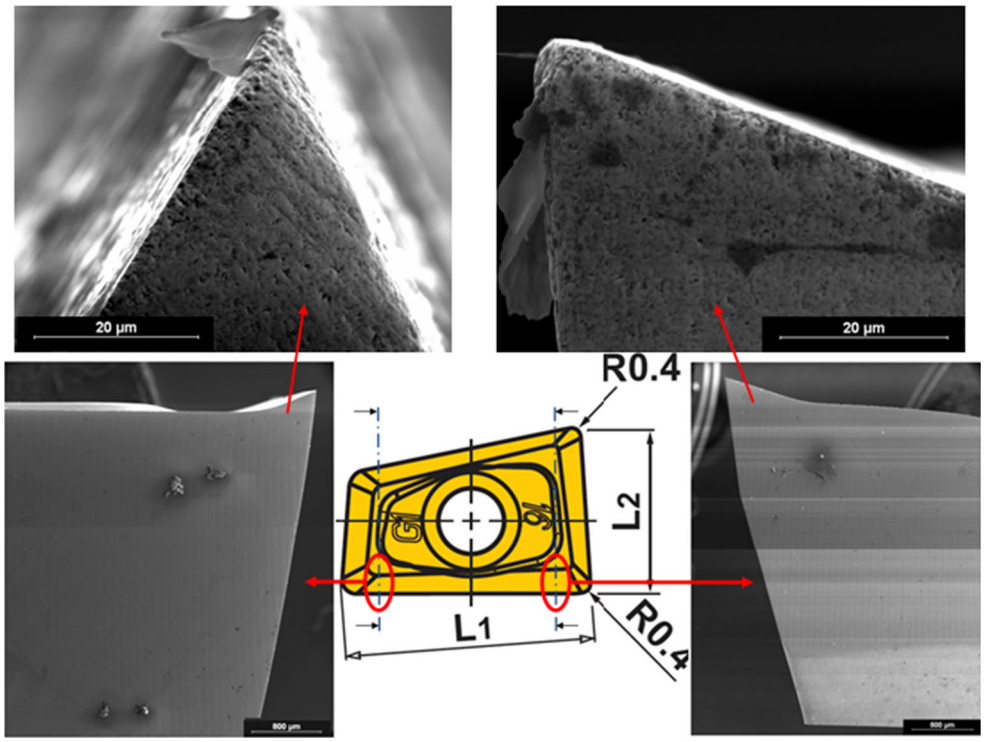

Fig. 3 Cutting edge of an insert on the AQX milling cutter

were ground so as to be able to observe their cutting edge in cross-section. These edges were studied in two locations as shown on Fig. 3. They were then observed under the SEM. These measurements also correspond to the sharpness measured using the 3D optical measurement system Alicona as shown on Fig. 4. For example, the sharpness measured with SEM for the HTi10 3 µm, and about 2.5 µm with the Alicona system.

The design of experiments bounds are shown in Table 1 for HTi10 insert.

Due to confidential issues, the values for the cutting speed Vc (m/min) and the feed per tooth fz (mm/rev/tooth) are not given. They are stated in forged E21 as a percentage of the cutting conditions Vc^* and f^* given by Mitsubishi for this tool in non-ferrous alloys (Table 1). In the paper, the cutting conditions of the forged E21 are then normed from -1 to $+1$ for the minimal and maximal values, and the conditions for the other two alloys are stated with the same norm as in forged E21. The maximum radial offset value ae_2 is chosen so that the scallop height (h) (Fig. 1) is slightly lower than the tolerances ($h < 0.3$ mm), and $ae_1 = \frac{1}{2}.ae_2$. Some tests were also performed with a third value of ae: this value noted ae_3 was chosen by the authorized limit of the cutting insert, and its value is about twice that of ae_2. It can be seen that the domain bounds are different in the three alloys with the HTi10 inserts. In forged MRI301F as in cast E21, the feed had to be limited below the maximal value used in forged E21, because of catastrophic break of the cutting insert radius. This break appears with $fz > -0.09$ in cast E21, and with $fz > +0.64$ in forged MRI301F. The insert tool nose radius seems to be the part most exposed to thermomechanical stresses, thus also making it the most fragile part. Indeed, the tool nose radius enters the material first and leaves it last. It is therefore the zone subject to most stress, at the two moments where cutting shows the greatest difficulties due to the narrowness of the chips [8]. Here, the full-material plunge milling configuration allows impacts relating to cutting discontinuity to be reduced, given that the cutter enters the material gradually. With the VP15TF inserts, the variation ranges of cutting conditions in the three alloys are the same as in wrought E21 with HTi10 inserts.

3 Cutting forces

The force measuring stage recorded the forces Fx, Fy, and Fz in its own fixed reference (x,y,z). These forces were then converted into the rotating reference of the cutter in order to obtain the tangential (Ft), radial (Fr) and axial (Fa) forces (Fig. 5). In the present instance, a single insert is mounted on the cutter so as to obtain only forces $Ft1$, $Fr1$ and $Fa1$ of Fig. 5. θ is the angle of engagement of the insert as shown on Fig. 2. The insert enters the material with an angle θ_e as given by Eq. 2, with ae the radial offset and R the milling cutter radius (Fig. 2).

Figure 6 shows an example of forces measured by the force measuring stage, as also the corresponding forces

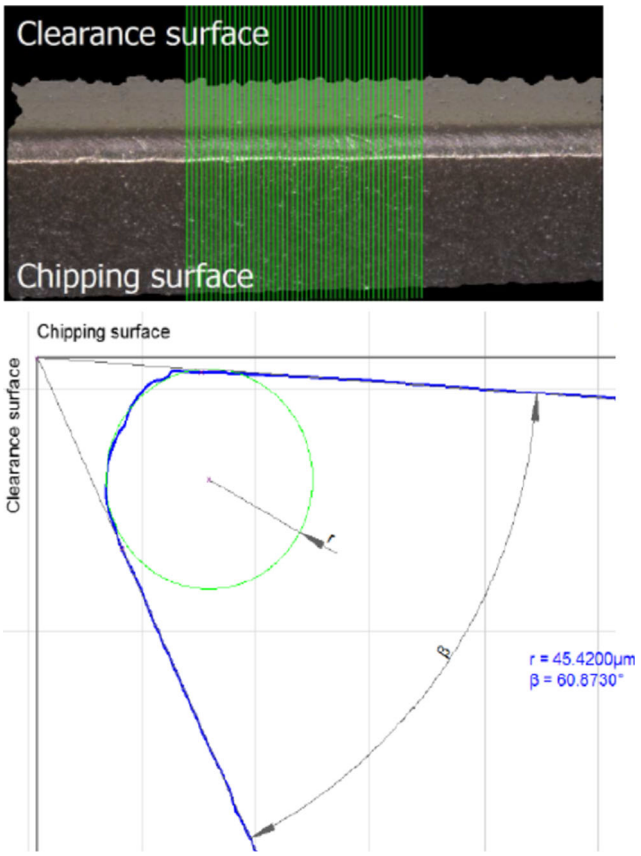

Fig. 4 Cutting edge of a VP15TF insert

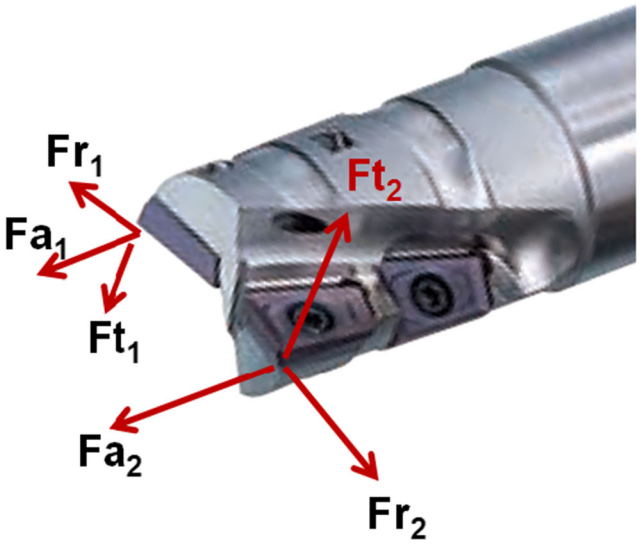

Fig. 5 Directions of forces related to each insert in the cutter reference

in the cutter rotating reference over three cutter rotations obtained with the Matlab software. For each test performed, frequency analysis was conducted in order to check whether disturbances appear. The filter chosen was a linear low-pass filter of the Butterworth type of order 4, characterised by a gain as constant as possible on the bandwidth.

3.1 Tangent force *Ft*

On Fig. 7 representing the change in maximum tangential force (averaged over three milling cutter rotations), it is easy to distinguish three separate clusters of curves each corresponding to a radial offset value ($ae1$ in orange, $ae2$ in green and $ae3$ in blue). In each of these clusters, all the cutting speed conditions Vc are merged, showing that the maximum force hardly depends on this parameter at all. However, it increases quite distinctly with the radial offset and with the feed per tooth. The equivalent curves for MRI303F and cast E21 are identical to those shown in Fig. 7, as shown on Fig. 8 for a cutting speed value of Vc-1. Figure 9 shows the maximum forces measured with the VP15TF inserts in forged E21 (with for purposes of comparison the corresponding curve derived from HTi10 inserts in forged E21). Note that similar values (difference between values is under 5 %) are obtained with the two other alloys and are not represented on Fig. 8 for sake of clarity. Thus, the maximum values measured with the VP15TF inserts are very much the same as with the HTi10 cutter (Fig. 9). Ft_{max} hardly depends at all on the cutting speed, the material or the type of insert, but just on the feed per tooth and the radial offset (and thus the chip cross-section): it can be seen that the points corresponding to the three alloys milled using the VP15TF inserts follow much the same evolution as for the forged E21 machined with the HTi10 inserts.

3.2 Radial force *Fr*

As explained in the bibliography [8, 10–12], the radial force is found to be considerably reduced with plunge milling

Table 1 Variation ranges of cutting conditions with HTi10 and VP15TF inserts

	Forged E21		Forged MRI301F	Cast E21
Cutting speed ***Vc***	80 to 200 % of Vc^*	−1 to +1	−1 to +1	−1 to +1
Feed per tooth ***fz*** HTi10	154 to 1690 % of f^*	−1 to +1	−1 to +0.64	−1 to −0.09
Feed per tooth ***fz*** VP15TF	154 to 1690 % of f^*	−1 to +1	−1 to +1	−1 to +1
Radial offset value ***ae***	ae_1, ae_2 and ae_3			

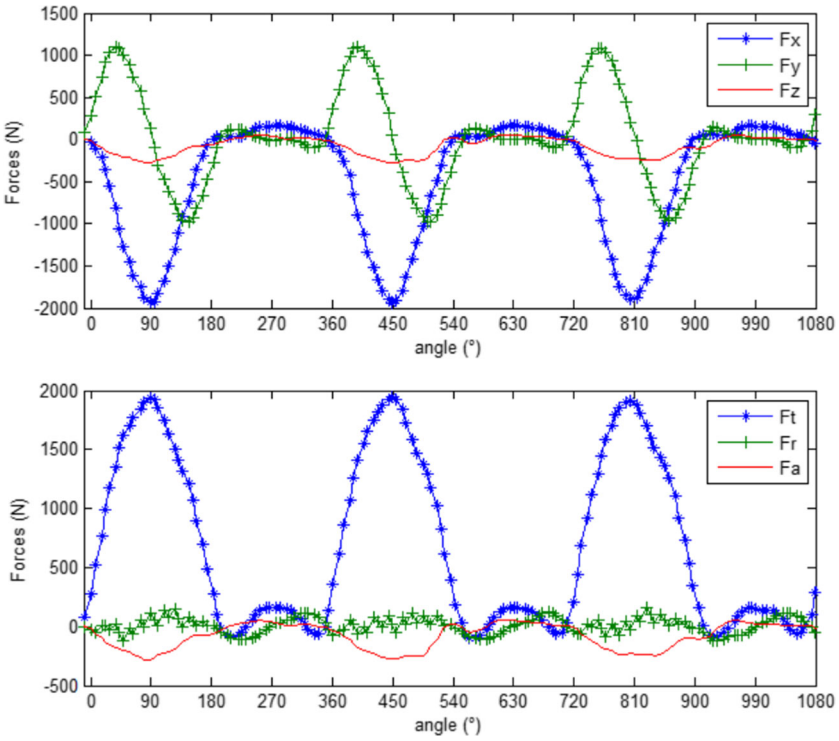

Fig. 6 Forces Fx, Fy and Fz obtained with the Kistler plate, and corresponding forces as calculated Ft, Fr and Fa over three cutter rotations

as compared with conventional milling operations. In this study, with the AQX milling cutter and these Mg-Zr-Zn-RE alloys, this force is quasi-inexistent. It can be seen for example on Fig. 6. This test illustration corresponds to a plunge milling with a HTi10 insert. Varying the cutting conditions does not change the evolution of Fr which remains near null. With the VP15TF cutter, the same phenomenon is observed: the radial force always remains near null for the three alloys. This radial force will therefore not be taken into account during the modelling.

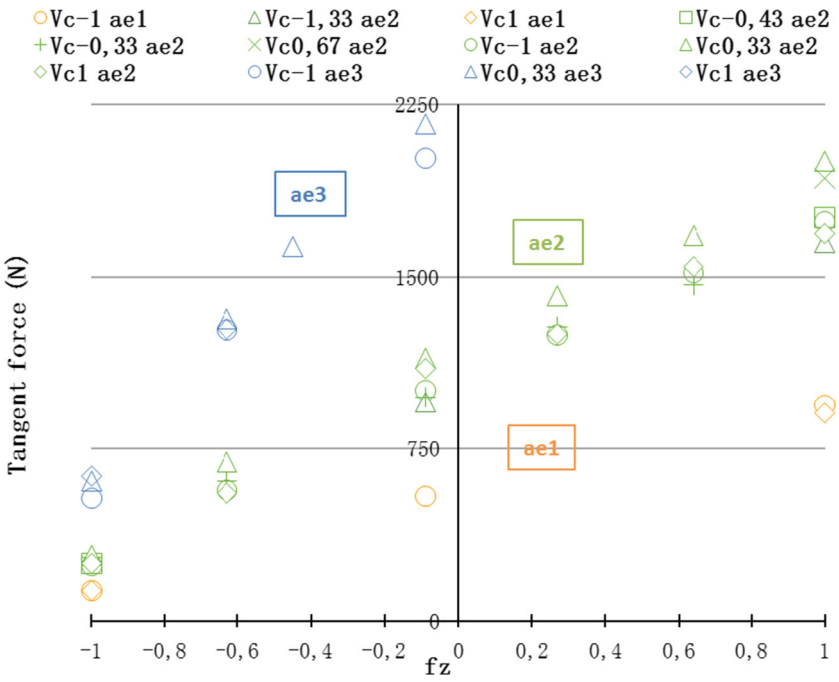

Fig. 7 Maximum tangential force in relation to the feed fz during plunge milling of forged E21 with HTi10 inserts. In the legend, Vc-1 $ae2$ corresponds to tests at Vc-1 and $ae2$ where the feed fz is varied

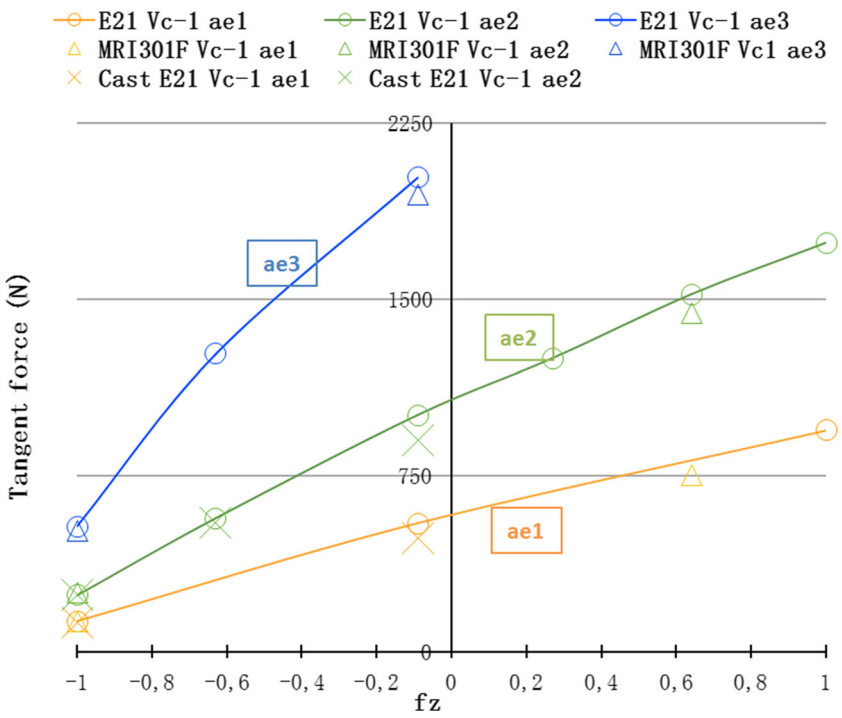

Fig. 8 Comparison of Ft force maxima in the three alloys at Vc-1 and different ae with HTi10 inserts. In the legend, Vc-1 $ae2$ corresponds to tests at Vc-1 and $ae2$ where the feed fz is varied

3.3 Axial force Fa

Figure 10 shows the evolution of the maximum axial force (averaged over three cutter rotations) in each alloy, according to the feed per tooth. MRI303F and cast E21 show exactly the same trends. The forces recorded in the case of forged E21 are a bit more significant. In all cases, it can be seen that with a low feed per tooth, the axial force is slightly positive, whereas it then becomes negative. It cannot be said that there is a linear evolution in relation to the

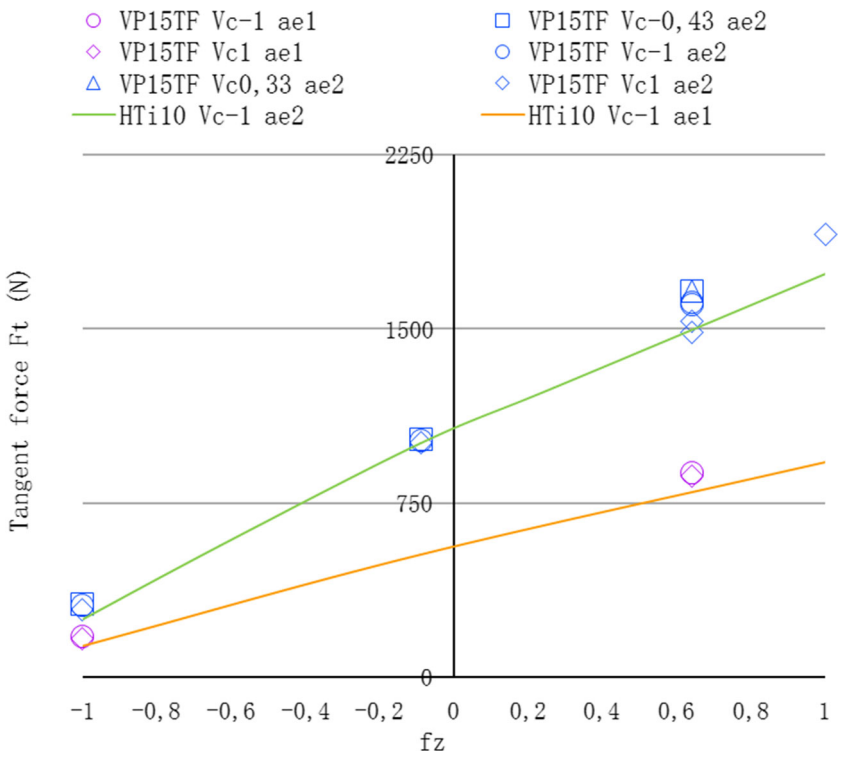

Fig. 9 Maximum tangential force in relation to the feed fz during plunge milling of forged E21 using VP15TF inserts (and, for comparison, with HTi10 in forged E21)

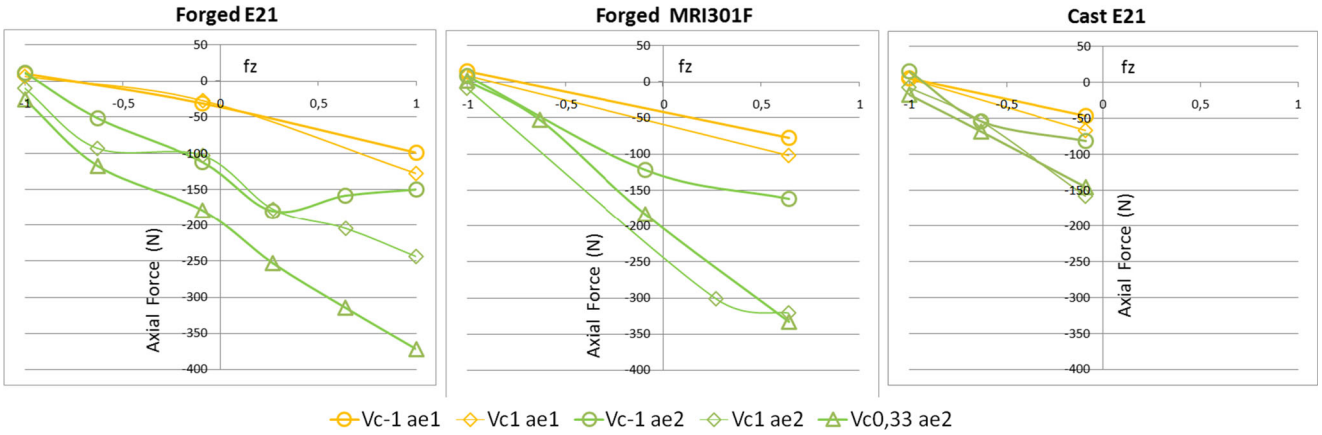

Fig. 10 Evolution of the maximum axial force in relation to the feed fz for each alloy milled using HTi10 inserts

cutting speed, given that the forces recorded at Vc+1 are to be found between those measured at Vc-1 and those at Vc+0.33. However, it appears obvious that the cutting speed has an influence on these axial forces. With the VP15TF insert, for the three alloys, the axial forces never become negative as with the HTi10 inserts. However, they tend to diminish slightly when the feed increases (Fig. 11).

3.4 Evaluation

It was seen that the cutting forces evolve in the three alloys in the same way. The maximum tangential force depends on the feed per tooth and the radial offset. For the maximum axial force, it would appear that the cutting speed also plays a role. Preparation of the cutter only seems to intervene in axial force, which is negative in the case of machining with HTi10 inserts for non-ferrous alloys (facilitating cutting by "sucking" the cutter downwards), and positive with VP15TF inserts. The temperature was not measured during the plunge milling tests. However, it was noticed that the chips remained cold enough to be touched without feeling a burning sensation as soon as the plunge was completed. Similarly, the workpiece did not seem to see an increase in temperature. This must be due to the extremely good thermal conductivity of magnesium, that allows heat to be evacuated into the rest of the mass of the workpiece.

4 Modelling the cutting forces

In order to be able to optimise cutting conditions, for example, it is essential to model the cutting forces. In production, knowledge of the cutting forces allows you to size the machining assemblies/machine-tool or machine power ratings needed for the process [12, 23].

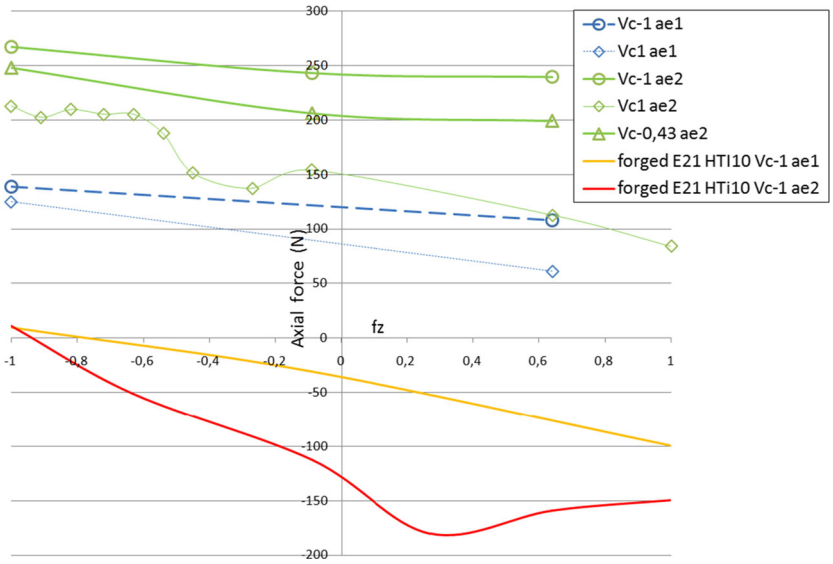

Fig. 11 Axial forces measured with the VP15TF insert in forged E21 (for purposes of comparison, the *orange* and *red curves* correspond to the HTi10 inserts in forged E21)

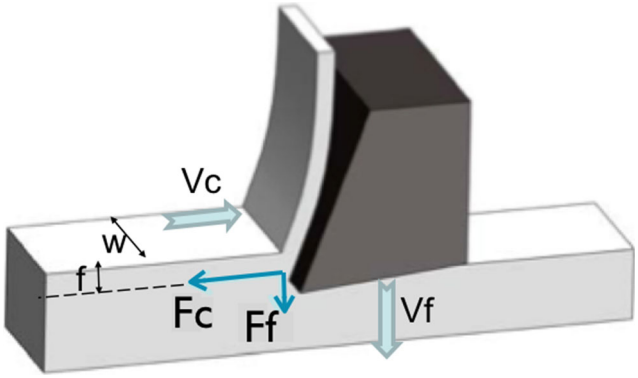

Fig. 12 Orthogonal cutting

4.1 Setting up the cutting forces model

When plunge milling different magnesium alloys, a number of special features may first be observed to serve as a guide in choosing the cutting model. It has been seen for example that the radial force is negligible, while Vc has an influence on the axial force Fa but not on the main force Ft. The temperature gradients seemed to be fairly weak such as not to disturb the model too much. Plunge milling, with the cutters used in the present study, fairly closely resembles orthogonal cutting, as will now be shown. In the case of plunge milling, it can be considered that the main cutting edge (the horizontal edge of length L1 on Fig. 3) is perpendicular to the cutting speed Vc and feed speed Vf thanks to the inserts showing a null radial rake angle. However, there is a secondary cutting edge (vertical edge) that also intervenes. This cannot therefore be considered to be a perfect case of orthogonal cutting. However, observation of the chips during plunge milling together with plunges filmed using a high speed camera showed that the horizontal edge was the only one to generate a chip, in crescent shape. The vertical edge comes into action as the cutter moves up and out, taking up the very fine material on the wall, which is the sign of a certain springback of the milled material.

These various observations led us to eliminate thermo-mechanical models and focus on a purely mechanical model of the Merchant type. Indeed, this type of modelling allows the cutting forces to be predicted in a simplified manner, without having a huge number of coefficients to be determined as in most models of cutting forces that take material behaviour or the thermal environment into account, for example.

The Merchant model [24, 25] was the first analytical model to describe the mechanics of orthogonal cutting (Fig. 12). It is based on certain assumptions: the cutting edge is perpendicular to Vc and Vf, the cutter edge radius is null, the chip width is constant, there is a shear plane, only primary shearing is taken into account, the cutter-chip interface is considered sliding with friction, the material shows plastic behaviour, Coulomb friction is constant. From these assumptions, it considers that chip formation occurs along a shear plane going along the tool's cutting edge and tilted by an angle Φ in relation to cutting speed.

HTi10 grade inserts have an extremely good sharpness and can validate a null edge radius. VP15TF grade QOGT1651R-G1 inserts meanwhile have an edge radius of about 45 µm, much bigger then and thus deviating from Merchant's hypothesis.

An adaptation of this model is then introduced, to be applicable to plunge milling and for the different grade inserts (HTi10 and VP15TF). This radius will be taken into account, in the modelling, through its impact on the apparent rake angle as it will be presented further.

In the present instance, the chip width is not constant, considering that it changes with each angle of engagement θ of the insert into the material (Fig. 2). The chip width will thus be variable, and defined by Eq. 3.

$$w(\theta) = R + ae.sin\theta - \sqrt{R^2 - ae^2.cos^2\theta} \tag{3}$$

It may therefore be considered a case of orthogonal cutting at each angular position.

In the present study, the Merchant shear plane angle Φ, defined in Eq. 4 will be considered.

$$\Phi = \frac{\pi}{4} - \frac{\varphi - \gamma}{2} \tag{4}$$

In this equation, γ represents the cutting angle. The angle of friction φ as well as the shearing stress τ are not here considered to be constant, contrary than Merchant's hypothesis. Thus, the system of Eq. 5 is obtained, with τ and φ the two

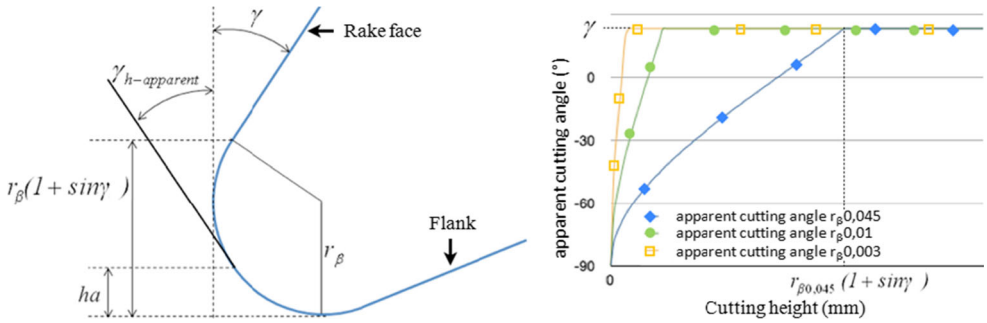

Fig. 13 Theoretical cutting angle γ and apparent cutting angle $\gamma_{h-apparent}$ (*left*) and changes in $\gamma_{h-apparent}$ (right)

unknowns of the system, by applying the Merchant model to each angular position of the insert:

$$\begin{cases} Fc = \dfrac{\tau.fz.w(\theta).cos(\varphi-\gamma)}{cos(\Phi+\varphi-\gamma).sin\Phi} \\ Ff = \dfrac{\tau.fz.w(\theta).sin(\varphi-\gamma)}{cos(\Phi+\varphi-\gamma).sin\Phi} \end{cases} \tag{5}$$

With the Φ value defined by Merchant (Eq. 4), this system may be reduced to the system (6).

$$\begin{cases} Fc = \dfrac{2.\tau.fz.w(\theta).cos(\varphi-\gamma)}{1-sin(\varphi-\gamma)} \\ Ff = \dfrac{2.\tau.fz.w(\theta).sin(\varphi-\gamma)}{1-sin(\varphi-\gamma)} \end{cases} \tag{6}$$

The goal is then to determine the couple (τ, φ) while minimising the gap between the experimental points of the tangential and axial forces (Ft_i and Fa_i) and the theoretical points given by system (5) (Fc_i and Ff_i). The indices i correspond to each angular position θ of the insert: Fc_i is thus the value of Fc measured at angle θ_i. This amounts to minimising the function (7).

$$W = \sum(Fc_i - Ft_i)^2 + \sum(Ff_i - Fa_i)^2 \tag{7}$$

To do so, the system of Eq. 8 has to be resolved, which amounts to resolving system (9), where : $A = \dfrac{1}{1-sin(\varphi-\gamma)}$.

$$\begin{cases} \dfrac{\partial W}{\partial \tau} = 0 \\ \dfrac{\partial W}{\partial \varphi} = 0 \end{cases} \tag{8}$$

$$\begin{cases} -2.\tau.fz.A.\sum(w_i^2) \\ \quad + cos(\varphi-\gamma)\sum(Ft_i.w_i) \\ \quad + sin(\varphi-\gamma)\sum(Fa_i.w_i) = 0 \\ -2.\tau.fz.A^3.cos(\varphi-\gamma).\sum(w_i^2) \\ \quad + A.\sum(Ft_i.w_i) \\ \quad + A^2.cos(\varphi-\gamma).\sum(Fa_i.w_i) = 0 \end{cases} \tag{9}$$

By applying this to the tests performed, for each test a couple (τ, φ) is obtained so as to have curves close to the experimental curves. The evolution of this couple now has to be checked in relation to the cutting parameters. The goal is seeing whether it is possible to find a generalisation and be able to model the forces encountered in a very large number of cutting condition configurations, from a minimum number of tests.

4.1.1 Taking into account the edge radius

Having a non-null edge radius entails a variation in the cutting angle all along the edge. Thus, there will be an apparent cutting angle $\gamma_{h-apparent}$ at each cutting height ha as illustrated in Fig. 13. This apparent cutting angle follows the expression (10), where γ is the cutting angle on the cutting face. $\gamma_{h-apparent}$ varies by $-90°$ to γ :

$$\begin{cases} if\, ha \geq r_\beta(1+sin\gamma)\, then: \\ \gamma_{h-apparent} = \gamma \\ if\, ha < r_\beta(1+sin\gamma)\, then: \\ \gamma_{h-apparent} = arcsin\left(\dfrac{ha}{r_\beta - 1}\right) \end{cases} \tag{10}$$

$$\begin{cases} fz \geq r_\beta(1+sin\gamma) & \gamma_{app,mean} = \dfrac{1}{r_\beta.(1+sin\gamma)}\displaystyle\int_0^{r_\beta(1+sin\gamma)} arcsin\left(\frac{ha}{r_\beta-1}\right)dha \\ & \gamma_{app,mean} = \dfrac{\sqrt{1-sin^2\gamma} + sin\gamma.arcsin\gamma - \pi/2}{1+sin\gamma} \\ fz < r_\beta(1+sin\gamma) & \gamma_{app,mean} = \dfrac{1}{r_\beta.(1+sin\gamma)}\displaystyle\int_0^{fz} arcsin\left(\frac{ha}{r_\beta-1}\right)dha \\ & \gamma_{app,mean} = \dfrac{\sqrt{1-sin^2(\frac{fz}{r_\beta-1})} + sin(\frac{fz}{r_\beta-1}).arcsin(\frac{fz}{r_\beta-1}) - \pi/2}{1+sin\gamma} \end{cases} \tag{11}$$

$$\begin{cases} fz \geq r_\beta(1+sin\gamma) & \gamma_{mean} = \dfrac{\gamma[fz - r_\beta(1+sin\gamma)] + \gamma_{app,mean}.r_\beta(1+sin\gamma)}{fz} \\ fz < r_\beta(1+sin\gamma) & \gamma_{mean} = \gamma_{app,mean} \end{cases} \tag{12}$$

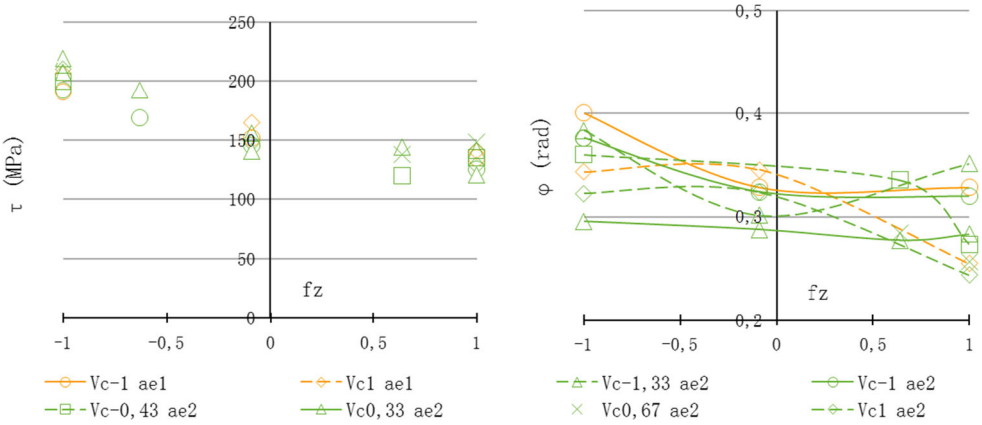

Fig. 14 Evolutions in shear stress τ and the angle of the cone of friction φ calculated by minimising at each instant the gap between the experimental and theoretical values of the axial and tangential forces in relation to the feed per tooth fz, in forged E21 machined using HTi10 inserts

Figure 13 (right) shows the change in the apparent cutting angle $\gamma_{h-apparent}$ for three different edge radii (0.045, 0.01 and 0.003 mm).

Albrecht was the first to integrate the edge radius into the Merchant model [26]. Part of his works are adopted here, also relating the edge radius to the cutting height to define a mean rake angle seen by the entire cutting edge in contact with the material. Indeed, according to the chosen feed per tooth fz, there will be a greater or lesser cutting height fraction in the edge radius. If a mean rake angle γ_{mean} is considered on the height machined fz, the latter must take into account the portion where there is γ, and that where there is $\gamma_{h-apparent}$. $\gamma_{app,mean}$ represents the mean rake angle seen in the edge radius (i.e. for a height $ha < r_\beta(1 + sin\gamma)$). Its value is given by the expression (11).

Thus, over the entire cutting height fz, there will be a mean rake angle γ_{mean} expressed as given by the expression (12).

The modified Merchant model can now be applied, that is taking into account the edge radius on calculation of the rake angle. The rake angle considered here is the mean rake angle γ_{mean} on the cutting height fz.

Coefficients τ and φ were calculated for all the tests performed. Thus, they can be studied in relation to the cutting parameters. The shear stress evolves according to a power function of the feed per tooth, as shown on Figs. 14 and 15. Whatever the cutting speed or radial offset, evolution of τ is the same, and can thus be expressed as in Eq. 13. The evolution of φ is more complex and seems to depend on several parameters at the same time (Fig. 14). It was decided to simplify the expression of φ, observing that this parameter appears to depend mainly on fz and Vc (Fig. 15). This angle of friction is thus expressed as shown in Eq. 13, where Vc_0 represents the minimum speed of the tests (i.e. here Vc-1).

$$\begin{cases} \tau = a.fz^b \\ \varphi = c.fz^d.\left(\dfrac{Vc}{Vc_0}\right)^e \end{cases} \tag{13}$$

It is thus possible to determine these various coefficients (a and b on the one hand, and c, d and e on the other) with just three tests chosen in the field of application of cutting conditions.

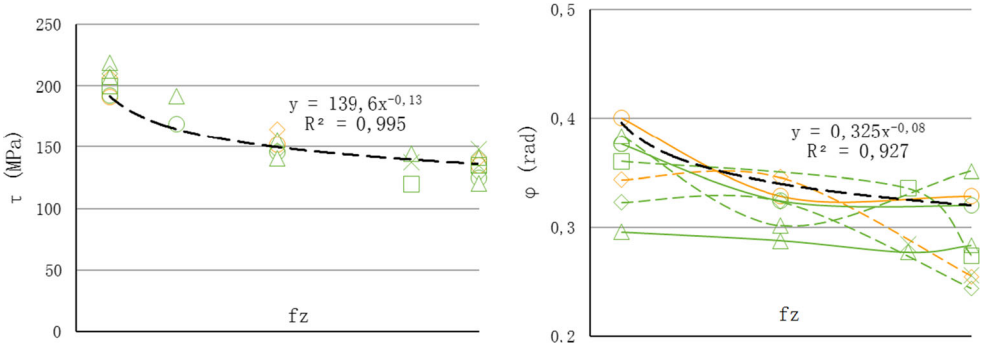

Fig. 15 Evolutions in shear stress τ and the angle of the cone of friction φ in relation to the feed fz, in forged E21 machined using HTi10 inserts. The indicative trend curves correspond to tests at Vc-1 and $ae1$

Table 2 Possible test combinations to determine coefficients a, b, c, d and e

	Combination 1			2			3			4		
	Vc	fz	ae	Vc	fz	ae	Vc	fz	ae	Vc	fz	ae
Test 1	−1	−1	+1	−1	−1	−1	−1	−1	+1	−1	−1	−1
Test 2	+1	+1	+1	+1	+1	+1	+1	+1	−1	+1	+1	−1
Test 3	inter	+1	+1	inter	+1	+1	inter	+1	+1	inter	+1	+1
	5			6			7			8		
	Vc	fz	ae	Vc	fz	ae	Vc	fz	ae	Vc	fz	ae
Test 1	−1	+1	+1	−1	+1	+1	−1	+1	−1	−1	+1	−1
Test 2	+1	−1	+1	+1	−1	−1	+1	−1	+1	+1	−1	−1
Test 3	inter	+1	+1	inter	+1	+1	inter	+1	+1	inter	+1	+1

4.1.2 Quality of the model

The problem now is to determine whether the choice of three tests allowing five coefficients to be obtained has an influence on the quality of the model. To do so, a limited statistical study is conducted. This involves choosing the first two tests necessarily on the domain boundaries and that must thus be conducted at Vc_{min} or Vc_{max}, fz_{min} or fz_{max} and ae_{min} or ae_{max}, knowing that they must have a different feed per tooth in order to be able to determine the coefficients a and b. The third test is chosen with an intermediate cutting speed, fz_{min} or fz_{max}, and ae_{max}. There thus remain eight possible test combinations, shown in Table 2 with the cutting condition boundaries (−1 for the minimum condition, and +1 for the maximum condition).

Each combination generates a different couple (τ, φ) to be integrated in the Merchant system of Eq. 6. The model thus obtained is then applied to the eight tests located at the domain boundaries, as well as to certain other intermediate tests. The deviation between the experimental value Ft_i and the theoretical value on the prevailing force (tangential force) at each instant is then considered.

Two types of errors are calculated:

- The mean error EFt : this is the mean for errors calculated at each instant between model and experimental EFT_i (for each angular position $45° < \theta < 135°$ in order to avoid possible issues where the chip is too thin).
- Error EFt_{max} on the maximum for tangential force

These two types of errors (Fig. 16) are calculated according to the system of expressions (14). It follows that it is in the case of cast E21 that the model generates the least errors and that the different combinations have little influence on those errors. In MRI301F, the first two combinations always generate less than 15 % of error, while in the other configurations, some tests at boundaries or within the domain show more than 20 % of error.

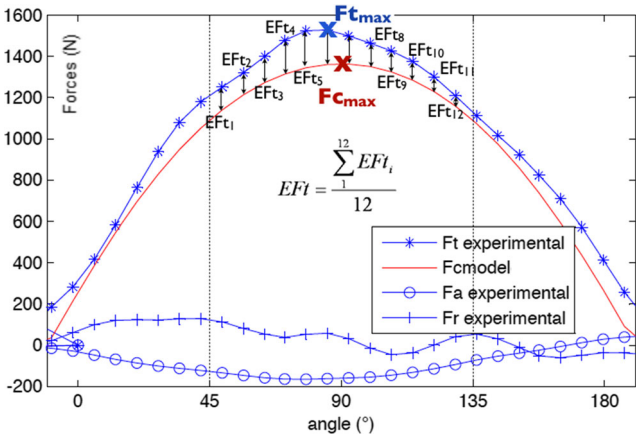

Fig. 16 Example of mean error calculation between 45 and 135° and representation of Ft_{max} and Fc_{max} for a test at Vc+0.67, fz+0.64 and $ae2$

$$\begin{cases} EFt_i = 100.\dfrac{|\ Ft_i - Fc_i\ |}{|\ Ft_i\ |} \\ EFt_{max} = 100.\dfrac{|\ Ft_{max} - Fc_{max}\ |}{|\ Ft_{max}\ |} \end{cases} \tag{14}$$

In the case of forged E21, combinations 7 and 8 give more significant errors at low Vc and low fz. The other combinations give acceptable errors always less than 20 %. Considering the results on the three alloys, it was decided always to use the second test combination in order to determine parameters a to e allowing τ and φ to be defined. This combination corresponds to the use of two limit tests: one test at Vc_{max}, fz_{max} and ae_{max}; one test at Vc_{min}, fz_{min} and ae_{min}. The third test must be done at an intermediate cutting speed, at fz_{max} and ae_{max}. Indeed, the same

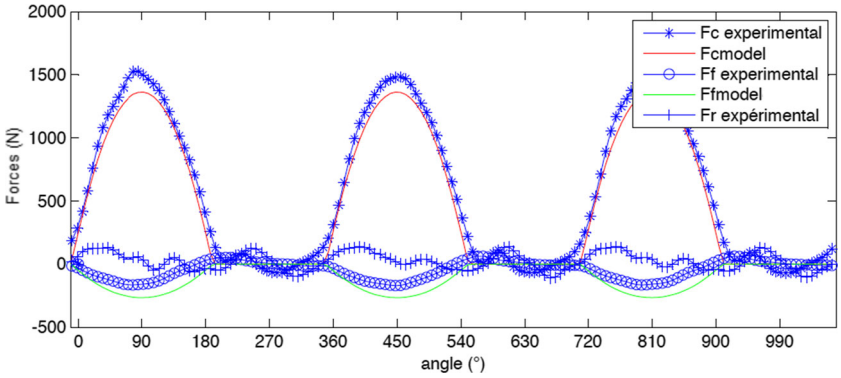

Fig. 17 Example of experimental curves and those from the cutting model for a test at Vc+0.67, fz+0.64 and $ae2$

approach was applied conducting the third test at an intermediate feed fz, and the model thus obtained in all cases gives extremely significant errors in all the alloys. In each alloy, it is thus possible to determine the various coefficients of the model, as indicated in Eqs. 15, 16 and 17 in order to inject them in Eq. 6.

$$\begin{cases} forged\ E21 \\ \tau = 137,83.fz^{-0,1644} \\ \varphi = 0,3453.fz^{-0,0801}.\left(\dfrac{Vc}{Vc_0}\right)^{-0,6189} \end{cases} \quad (15)$$

Table 3 Errors between the model and experimental forces on the tangential force Fc (%) and on the axial force Ff (N) in the three alloys machined using HTi10 inserts (green values are acceptable, not red values)

Forged E21

Vc	fz	ae	γ_{mean} (°)	E Fc_{moy} (%)	E Fc_{max} (%)	E Ff_{moy} (N)	E Ff_{min} (N)
1	1	ae2	22,2	6,43	2,49	66	101
1	1	ae1	22,2	13,29	12,77	14	51
-1	1	ae2	22,2	6,69	5,66	69	1
-1	1	ae1	22,2	1,41	0,94	28	23
1	-1	ae2	19,5	14,74	13,57	15	18
1	-1	ae1	19,5	4,65	3,79	10	8
-1	-1	ae2	19,5	4,65	3,79	10	1
-1	-1	ae1	19,5	1,4	2,41	3	4
-0,43	1	ae2	22,2	1,24	2,21	11	95
-0,43	-1	ae2	19,5	4,71	4,3	7	15
0,67	1	ae2	22,2	14,56	16,85	41	34
-1,33	-1	ae2	19,5	8,44	6,99	33	24
-1,33	1	ae2	22,2	17,12	18,79	89	11
-1,33	-0,09	ae2	22	21,85	18,34	120	24
0,67	0,64	ae2	22,2	8,92	9,42	101	65
0,67	0,64	ae1	22,2	11,42	13,13	48	36
1	-0,09	ae2	22	10,06	14,27	103	6
1	-0,09	ae1	22	22,28	24,35	60	10
-1	-0,09	ae2	22	4,69	2,85	16	26
-1	-0,09	ae1	22	1,64	1,98	7	13

Forged MRI301F

Vc	fz	ae	γ_{mean} (°)	E Fc_{moy} (%)	E Fc_{max} (%)	E Ff_{moy} (N)	E Ff_{min} (N)
1	0,64	ae2	22,2	8,97	1,38	15	50
1	0,64	ae1	22,2	10,32	7,38	29	41
-1	0,64	ae1	22,2	2,90	0,16	18	1
-1	0,64	ae2	22,2	4,59	4,23	18	2
1	-1	ae2	19,5	9,22	6,13	12	9
1	-1	ae1	19,5	11,31	7,77	11	9
-1	-1	ae2	19,5	2,52	3,63	3	0
-1	-1	ae1	19,5	1,74	2,40	2	4
0,33	0,64	ae2	22,2	8,43	10,07	30	101
0,33	-0,09	ae2	22	4,56	8,55	13	54
0,33	-0,64	ae2	21,5	4,67	8,04	10	31
0,33	-1	ae2	19,5	5,90	8,26	13	28

Cast E21

Vc	fz	ae	γ_{mean} (°)	E Fc_{moy} (%)	E Fc_{max} (%)	E Ff_{moy} (N)	E Ff_{min} (N)
1	-0,09	ae2	22	8,28	1,30	5	49
1	-0,09	ae1	22	7,89	4,80	6	11
-1	-0,09	ae2	22	2,05	2,77	58	4
-1	-0,09	ae1	22	5,04	4,57	25	6
1	-1	ae2	19,5	7,72	4,58	18	6
1	-1	ae1	19,5	7,67	0,43	6	3
-1	-1	ae2	19,5	2,31	3,08	3	6
-1	-1	ae1	19,5	0,62	1,00	1	2
0,33	-0,09	ae2	22	3,95	5,63	11	2
0,33	-0,64	ae2	21,5	2,00	3,77	8	0
0,33	-1	ae2	19,5	2,86	4,43	14	11
1	-0,64	ae2	21,5	8,52	1,10	6	2
-1	-0,64	ae2	21,5	1,84	0,35	8	20

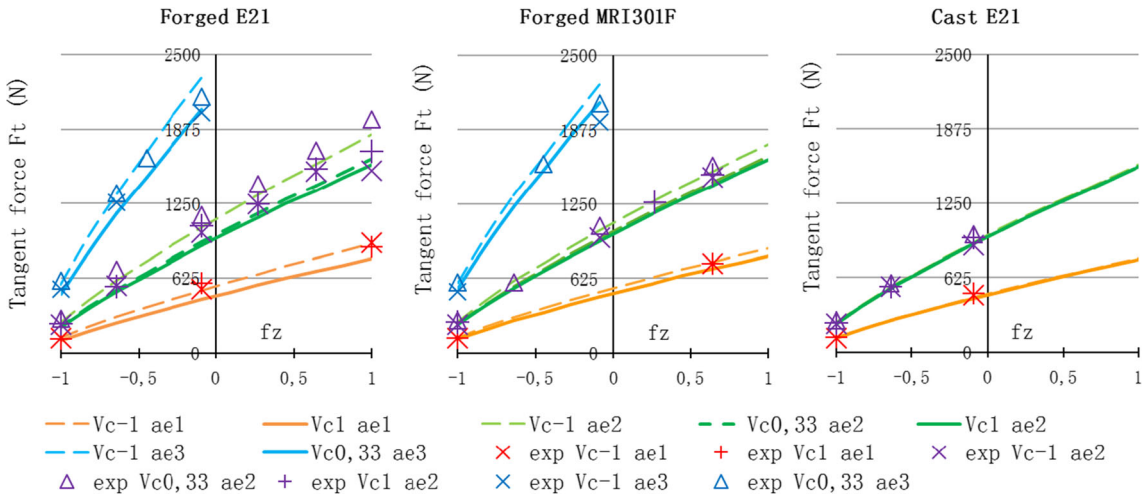

Fig. 18 Comparison of maximum values for the tangential force derived from the model and experimentation (exp)

$$\begin{cases} forged\ MRI301F \\ \tau = 135,81.fz^{-0,1698} \\ \varphi = 0,3059.fz^{-0,1445}.\left(\dfrac{Vc}{Vc_0}\right)^{-0,3306} \end{cases} \tag{16}$$

$$\begin{cases} cast\ E21 \\ \tau = 137,61.fz^{-0,1608} \\ \varphi = 0,2013.fz^{-0,2734}.\left(\dfrac{Vc}{Vc_0}\right)^{-0,0747} \end{cases} \tag{17}$$

4.2 Experimental validation of the cutting forces model

4.2.1 Application to tests with Hti10 inserts

It is now necessary to validate the model over all tests, looking at the deviation between experimental value and theoretical value of the model, both on the tangential force and on the axial force (Fig. 17). Over the entire domain of cutting parameters, error on the main force, the tangential force, is less than 15 %. On the axial force, it is not rational to express the error as a percentage when Fa is very close to 0, as the least error of a few Newtons will then massively increase the percentage. This explains why the errors in Table 3 are expressed as a percentage in the case of tangential force Fc in accordance with expressions (14), and in Newtons in the case of the axial force Ff, according to expression (18). In this expression, Fa corresponds to the experimental values of the axial force, and Ff represents the axial force calculated by the model. As for the tangential force, the mean error considered is the mean of EFf_i values for an engagement of the insert in the material between 45 and 135°. The minimum value of the axial force will be

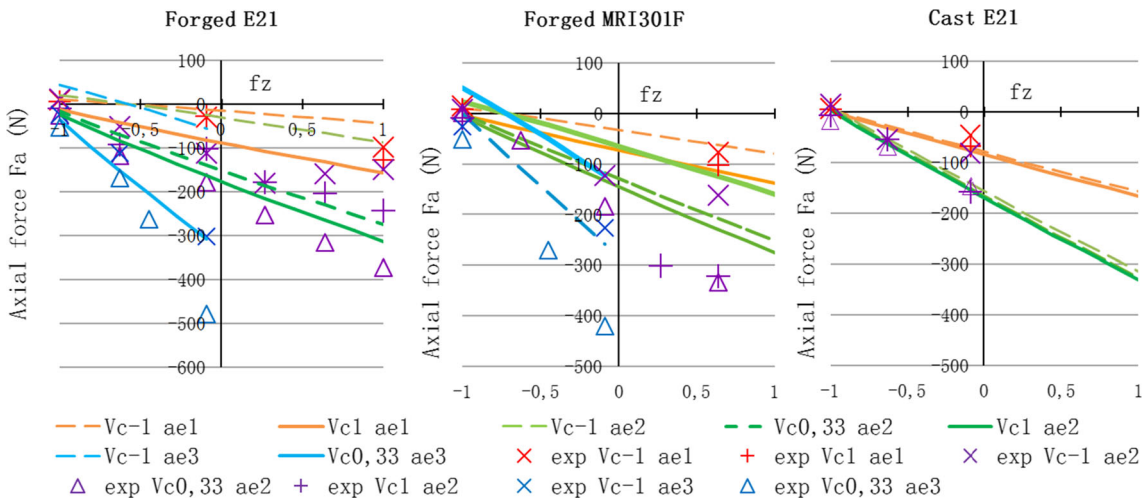

Fig. 19 Comparison of maximum values for the axial force derived from the model and experimentation (exp)

Table 4 Model setting tests for each alloy machined with the VP15TF inserts, with the couple (τ, φ) calculated for each of them

	Vc	fz	ae	forged MRI301F		forged E21		cast E21	
				τ	φ	τ	φ	τ	φ
Test 1	Vc1	fz0.64	ae2	117.22	0.3426	118.21	0.3434	118.74	0.3437
Test 2	Vc-1	fz-0.1	ae1	124.08	0.1996	138.84	0.1203	133.31	1755
Test 3	Vc0.33	fz0.64	ae2	124.64	0.3804	127.28	0.3468	119.61	0.3565

taken when it is negative, and its maximum value when it is positive (at low feed).

$$\begin{cases} EFf_i = \mid Fa_i - Ff_i \mid \\ EFf_{min} = Ff_{min} - Fa_{min} \end{cases} \quad (18)$$

It can be seen for the three materials presented in Table 3 that error on the tangential force is always fairly low, whether on the maximum value or on the remainder of the milling cutter's rotation. In cast Elektron 21, the mean error between 45 and 135° is thus less than 9 % over the entire cutting domain, while the error on the maximum remains below 5 %.

In this alloy, the axial force is also correctly modelled as the error generated generally remains below 25 N. These results are similar to those for MRI301F where the mean error on Fc does not exceed 12 % and the error on the maximum value for Fc does not exceed 10 %. The mean error on the axial force remains acceptable given that it is always less than 30 N. As for the error on the minimum value of Ff, this may reach fairly significant values. In forged Elektron 21, the mean error is less than 15 % on the tangential force within the domain, but can reach slightly higher values for tests outside the domain. However, the model does not allow the value of the axial force to be predicted successfully as it often reaches more than 50 N of error. However, the positive or negative trend of this axial force is well represented in all cases.

The fact that the model seems to work in cast E21 can be explained by the fact that the cutting conditions domain is more restricted ($fz_{max_{E21cast}} = 0,5.fz_{max_{E21forged}}$). Furthermore, no test outside the domain was conducted in the case of cast E21 and forged MRI301F.

Figure 18 shows the maximum values for the tangential force derived from the model and experimentation for the three alloys. It is important to note that the models, although calibrated from tests performed at $ae1$ and

Table 5 Errors between the model and the experimental forces (VP15TF inserts) on the tangential force Fc (%) and on the axial force Ff (N) in the 3 alloys)

Forged E21

Vc	fz	ae	γ_{mean} (°)	E Fc_{moy} (%)	E Fc_{max} (%)	E Ff_{moy} (N)	E Ff_{min} (N)
1	0,64	ae2	17,51	6,94	0,72	7	52
1	0,64	ae1	17,51	12,98	15,18	10	33
1	-1	ae2	-31,89	16,94	19,57	37	46
1	-1	ae1	-31,89	8,9	4,75	12	12
-1	0,64	ae2	17,51	4,19	6,96	86	155
-1	0,64	ae1	17,51	9,97	15,15	50	97
-1	-1	ae2	-31,89	14,32	12,01	9	12
-1	-1	ae1	-31,89	5,4	0,03	3	1

Vc	fz	ae	γ_{mean} (°)	E Fc_{moy} (%)	E Fc_{max} (%)	E Ff_{moy} (N)	E Ff_{min} (N)
-1	-0,09	ae2	13,85	9,59	10,04	181	207
-0,43	-1,00	ae2	-31,9	8,80	10,35	24	30
-0,43	-0,09	ae2	13,85	9,71	10,92	167	175
-0,43	0,64	ae2	17,51	6,04	10,73	81	130
0,33	0,64	ae2	17,51	6,88	11,72	30	120
1	-0,09	ae2	13,85	11,19	10,34	142	147
1	1,00	ae2	18,43	4,92	7,26	41	10

Forged MRI301F

Vc	fz	ae	γ_{mean} (°)	E Fc_{moy} (%)	E Fc_{max} (%)	E Ff_{moy} (N)	E Ff_{min} (N)
-1	-1	ae1	-31,9	4,98	2,62	2	1
-0,43	0,64	ae2	17,5	3,59	0,11	31	27
0,33	0,64	ae1	17,5	12,40	12,52	26	61
0,33	0,64	ae2	17,5	5,51	7,61	28	91
1	0,64	ae2	17,5	7,66	5,58	42	71
1	0,64	ae2	17,5	6,36	1,60	32	50
1	1	ae1	18,4	8,49	10,09	24	66

Cast E21

Vc	fz	ae	γ_{mean} (°)	E Fc_{moy} (%)	E Fc_{max} (%)	E Ff_{moy} (N)	E Ff_{min} (N)
-1	-0,98	ae1	-29,28	4,86	2,78	4	3
-1	-1	ae2	-31,89	12,80	14,80	55	60
-0,43	0,64	ae2	17,51	2,61	2,48	68	94
0,33	0,64	ae2	17,51	3,48	4,85	9	83
1	-0,04	ae2	14,29	7,67	5,08	95	97
1	0,35	ae2	16,47	5,41	3,12	35	58
1	0,64	ae2	17,51	4,04	1,03	7	32
1	1,11	ae2	18,64	11,01	11,89	75	24

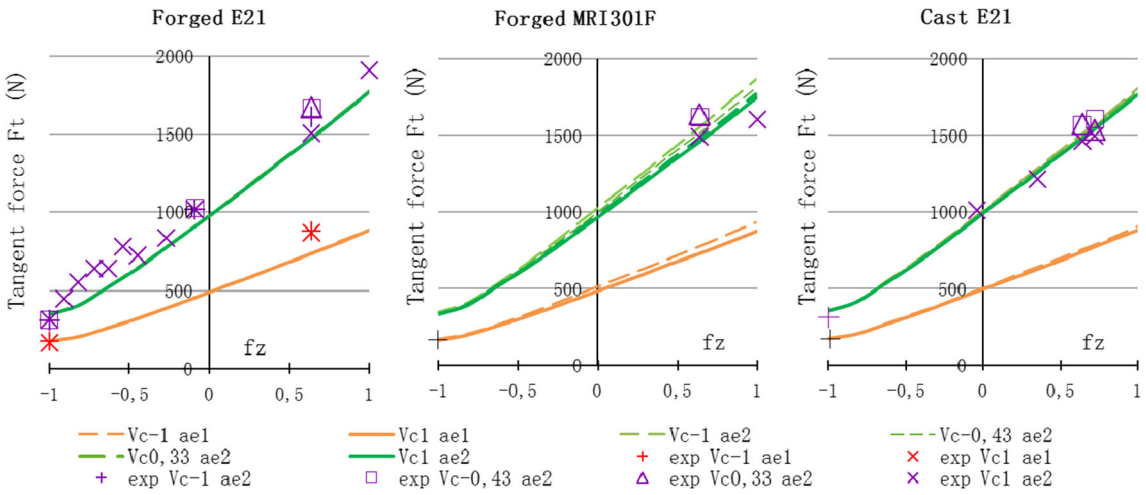

Fig. 20 Comparison of maximum values for the tangential force derived from the model and experimentation (exp) with VP15TF inserts

*ae*2, fairly closely represent the tests performed at *ae*3. The models, as also the tests, for forged alloys show a greater distinction between the cutting speeds as compared with the model and tests for the cast alloy that show very similar curves for different cutting speeds. This shows that the cast alloy is less sensitive to variation in the cutting speed.

Figure 19 shows maximum (or minimum according to the sign) values for the axial force in the same way, as derived from the model or experimentation. There is a greater disparity in the experimental values for this force. Moreover, it can be seen, especially in the case of forged alloys, that the model curves do not faithfully represent the experimental points. As was assumed when the study into errors between the model and experimental points was conducted, the model nevertheless satisfactorily shows the positive or negative trend of that force. The axial force is correctly modelled in the case of the cast alloy. In all cases, the differences between the results from the models and experimentation are not really significant in terms of forces.

4.2.2 Application Of The Modelling Method Implemented For Vp15Tf Inserts

Replacing the insert with one having a greater edge radius can change the model's performance. As compared with what was previously the case, the only Merchant assumption brought into question is that of the null edge radius. However, this difference was also catered for by introducing a mean rake angle γ_{mean} on the cutting height fz.

Here, the method described previously and refined with the HTi10 insert will be applied. This involves conducting three tests (one in maximum conditions, one in minimum conditions and one at intermediate Vc and fz and ae

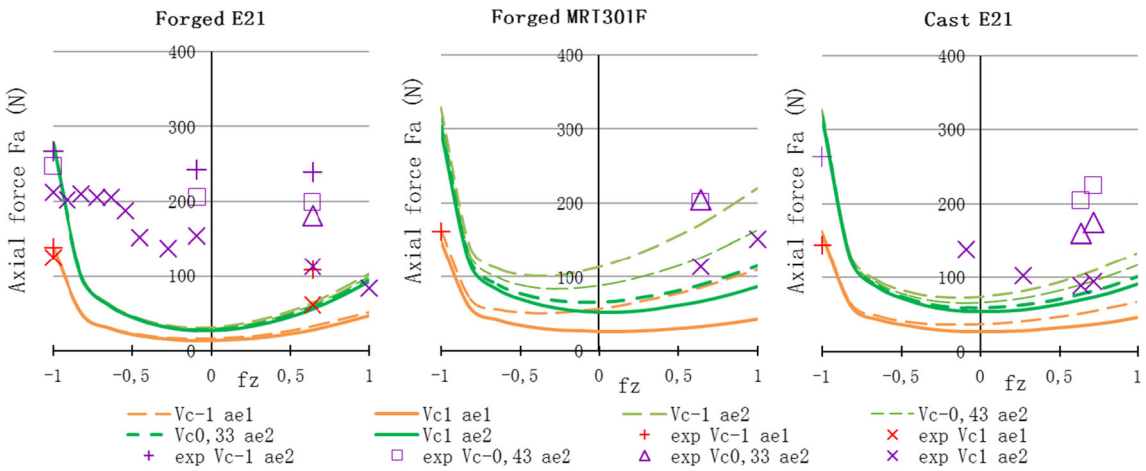

Fig. 21 Comparison of maximum values for the axial force derived from the model and experimentation (exp) with VP15TF inserts

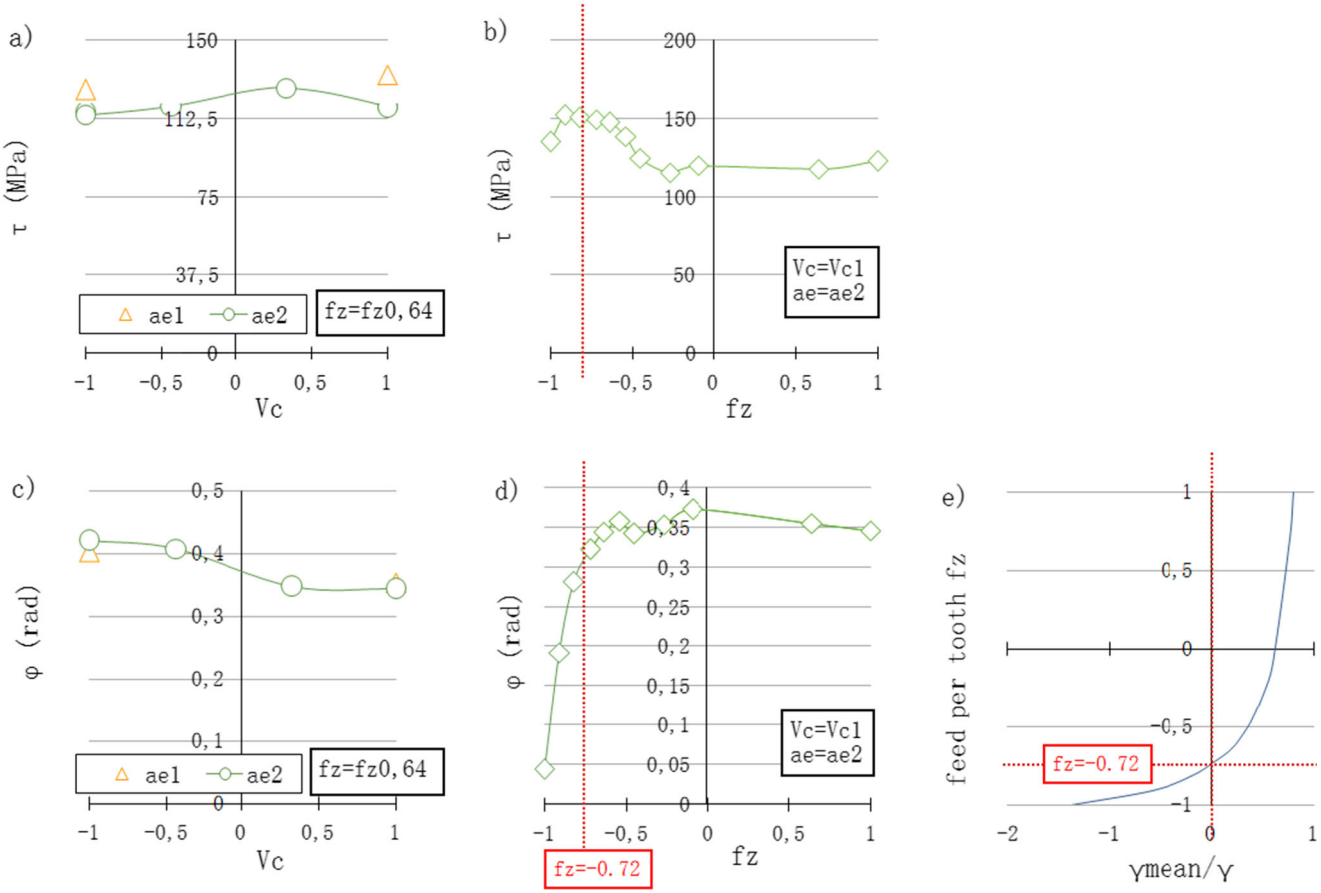

Fig. 22 Variation in the shear stress τ and the angle of friction φ in relation to the cutting speed (**a**, **c**) and the feed per tooth (**b**, **d**) in the case of forged E21 milling with VP15TF inserts, and evolution of the feed per tooth in relation to the ratio γ_{mean}/γ (**e**)

maximum). This is applied to the three alloys. It is considered that fz_{max}=fz+0.64, even though the feed per tooth was taken as far as fz+1 as the latter is very close to the insert ploughing conditions, and it was thus decided to set the model at a slightly lower feed. With these inserts, the maximum conditions are the same in all three alloys (Table 4).

Thus, for each alloy coefficients a, b, c, d and e of system (13) are obtained

$$\begin{cases} forged\ E21 \\ \tau = 118,2114.fz^{-0,0698} \\ \varphi = 0,3490.fz^{0,4625}.\left(\dfrac{Vc}{Vc_0}\right)^{-0,0175} \end{cases} \quad (19)$$

$$\begin{cases} forged\ MRI301F \\ \tau = 117,2243.fz^{-0,0247} \\ \varphi = 0,4063.fz^{0,3087}.\left(\dfrac{Vc}{Vc_0}\right)^{-0,1862} \end{cases} \quad (20)$$

$$\begin{cases} cast\ E21 \\ \tau = 118,7447.fz^{-0,0514} \\ \varphi = 0,3648.fz^{0,3178}.\left(\dfrac{Vc}{Vc_0}\right)^{-0,0650} \end{cases} \quad (21)$$

These values for (τ, φ) were then injected into system (6), that is itself applied to the various tests conducted with the VP15TF inserts. The errors for each test were then carried over into Table 5 in the same way as previously in Table 3. It can be seen as before that the

Table 6 New model setting tests with fz_{min}=fz-0.72 and new expressions of τ and φ

Vc	fz	ae	τ	φ	New expressions of τ and φ
Vc1	fz-0.72	ae2	149.51	0.3226	$\begin{cases} \tau = 118.21.fz^{-0.1694} \\ \varphi = 0.4770.fz^{0.0451}.\left(\frac{Vc}{Vc_0}\right)^{-0.3585} \end{cases}$
Vc1	fz0.64	ae2	118.21	0.3434	
Vc-1	fz-0.09	ae2	112.69	0.4661	

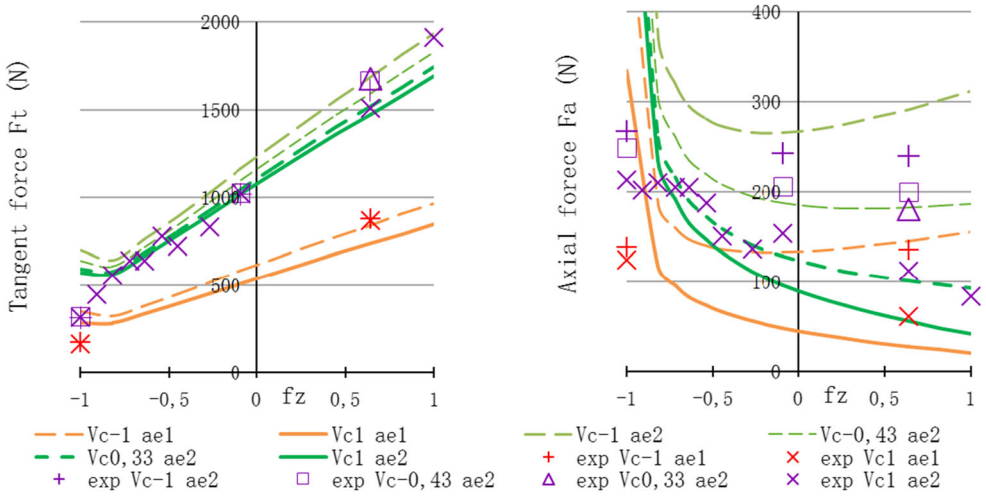

Fig. 23 Comparison of maximum values for axial and tangential forces derived from modelling and experimentation (exp) when machining forged E21 with VP15TF inserts

preponderant force, the tangential force Fc, is fairly well represented, given that in the three alloys errors on the maxima for Fc and over the entire curve (between 45 and 135°) are less than 15 %. However, the axial force Ff is less successfully modelled, with deviations that regularly reach more than 50 N, and even sometimes more than 100 N.

As with the HTi10 inserts, the maximum values for the tangential force are shown in Fig. 20. The points are derived from the tests while the curves represent the models, in each alloy. A good correlation can be seen between the experimental values and those drawn from the model for the tangential force. For the axial force, significant deviations are to be found between the model and tests (Fig. 21). This may be due to a poor approximation of the evolution of the angle of friction φ in relation to the cutting conditions.

Table 7 Errors between the model (set for fz_{min}=fz-0.72) and the experimental forces (VP15TF inserts) on the tangential force Fc (%) and on the axial force Ff (N) in forged E21

Forged E21							
Vc	fz	ae	γ_{moyen} (°)	E Fc_{moy} (%)	E Fc_{max} (%)	E Ff_{moy} (N)	E Ff_{min} (N)
1	0,64	ae2	17,51	6,94	0,72	7	52
1	0,64	ae1	17,51	12,98	15,18	10	33
1	-0,09	ae2	13,85	8,56	0,65	19	40
1	-0,27	ae2	12,02	14,1	8,22	20	26
1	-0,45	ae2	9,28	11,2	8,16	15	19
1	-0,54	ae2	7,32	3,6	7,2	29	41
1	-0,64	ae2	4,7	4,5	9,6	29	35
1	-0,72	ae2	1,04	3,2	4,6	10	14
1	-0,82	ae2	-4,45	7,5	1,2	25	29
0,33	0,64	ae2	17,51	5,04	9,46	45	80
-0,43	-0,09	ae2	13,85	8,72	7,26	21	19
-0,43	0,64	ae2	17,51	3,3	4,42	30	16

4.3 Limits of the cutting forces model and possible improvement

It has just been seen that the model provided a poor representation of the axial forces caused by the VP15TF inserts. This model was determined taking the three setting tests defined previously (maximum conditions, minimum conditions and intermediate Vc) and changes in τ and φ in relation to power functions of the feed per tooth, as stated in expressions (19), (20) and (21).

Evolution of the couple (τ, φ) when machining forged E21 (for which a large number of tests were conducted) with VP15TF inserts will now be considered.

The shear stress τ does not appear to vary in relation to the cutting speed Vc, but varies slightly in relation to fz and ae (Fig. 22a, b), as in the cases of HTi10 inserts. It can therefore be considered that the stress is correctly modelled, especially when fz is greater than fz-0,72 (Fig. 22b). The angle of friction φ varies slightly in relation to Vc (Fig. 22c), and varies hugely with the feed per tooth, as is show by Fig. 22d, but in a way that is extremely remote from a power function at low feed per tooth. It is thus necessary to limit the minimum feed considered in the model. The minimum feed per tooth thus chosen corresponds to fz-0.72, which in turn corresponds to the moment when the ratio $\frac{\gamma_{mean}}{\gamma}$ becomes positive (Fig. 22e).

The model determined in this section as well as the definition method with which it is associated is thus only valid over a restricted feed domain, such that $\frac{\gamma_{mean}}{\gamma}$ null defines

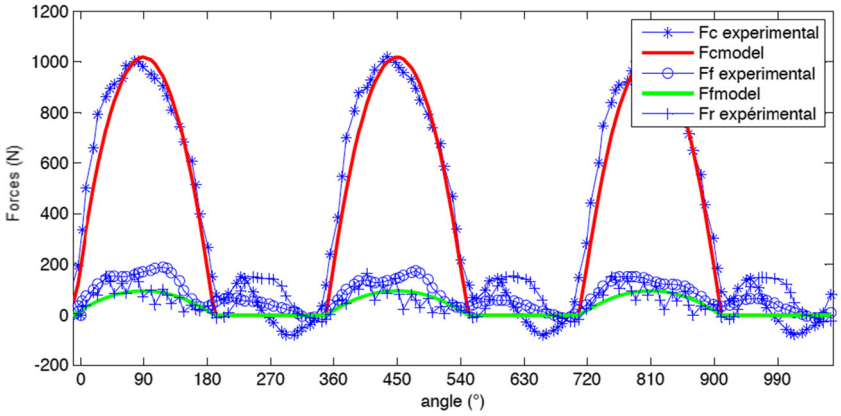

Fig. 24 Curves for experimental forces derived from the model (set for fz_{min}=fz-0.72) with VP15TF inserts (cutting parameters : Vc1, fz-0.09, ae2) (76 N of error on the axial force)

a new minimum value for the feed per tooth. The model setting test determined in minimal conditions must take into account this new lower limit for fz.

It can also be seen that reducing the mean rake angle allows the coefficient of friction brought into effect between the rake face and the chip during cutting to be reduced considerably as soon as γ_{mean} changes sign in relation to γ. Thus, as Fang showed during orthogonal cutting of lead-antimony alloys, a reduction of the coefficient of friction is obtained when the absolute value of the rake angle increases [27]. According to that author, the change would be symmetrical for a negative rake angle and a positive rake angle. In the present instance, this evolution does not appear to be symmetrical. Thus, if the method is now applied over the restricted domain, new coefficients are obtained for expressions of φ and τ (Table 6).

With these new expressions of φ and τ, the following curves to correlate experimental values and those derived from the model of axial cutting forces (Fig. 23) are obtained. The tangential forces are then correctly modelled and the axial forces are distinctly better represented than before, except when the feed is not high enough for $\frac{\gamma_{mean}}{\gamma} > 0$.

The forces modelled from this new setting of the model better show the axial and tangential forces inside the domain (Table 7).

Figure 24 shows an example of curves of experimental forces derived from the model so adapted.

5 Conclusions

- The preponderant force is the tangential force. This remains very close between the different magnesium alloys milled, but is particularly influenced by the feed per tooth and radial offset. It hardly depends at all on the cutting speed. The maximum tangential force is equivalent with the HTi10 sharp edged polished inserts and the VP15TF coated inserts with a greater edge radius.
- With the AQX milling cutter and these Mg-Zr-Zn-RE alloys, the radial force is quasi-inexistent. Varying the cutting conditions do not change the evolution of Fr which remains near null. Whatever the insert used, the same phenomenon is observed: the radial force always remains near null. This confirms that plunge milling behaves like orthogonal cutting with the type of cutter used.
- The maximum (if it is positive) or minimum (if negative) axial force follows the same evolution in the three alloys studied, but its values are higher in the case of forged E21. The axial force is slightly positive at low feed per tooth and switches to negative when the feed per tooth increases, seeing the absolute value of the force increase with it in the case of HTi10 inserts: the cutter is thus as if "sucked in" in the direction of the plunge. With the VP15TF inserts, the axial force is always positive, which indicates absence of this suction phenomenon, but diminishes with the increase in feed per tooth. This force is thus sensitive to the alloy, to preparation of the cutting edge, to radial offset, to the feed per tooth and to the cutting speed.
- To successfully optimise cutting conditions, they first need to be modelled. Merchant's orthogonal cutting model was thus adapted to represent these axial and tangential cutting forces. A methodology was devised so as to satisfactorily predict the cutting forces ($<$ 15 % on the preponderant force) over a broad range of cutting conditions from just three instrumented tests. This model is applicable as from a certain feed per tooth threshold determined thanks to the inequation $\gamma_{mean}/\gamma > 0$ in order to take the non-null edge radius of the cutting inserts into account.

– This study enable us to settle down an analytical cutting force model in plunge milling of three representative magnesium-rare earth alloys in aerospace industry. It will be interesting now to study if this model can be also used in the case of Mg-Al alloys that are widely used in aerospace industry. This work is currently in progress.

Acknowledgments The authors would like to thank the CARAIBE project, which is supported by national funds (FUI) and the AEROSPACE VALLEY cluster.

References

1. Gilles P, Monies F, Rubio W (2006) Modelling cutting forces in milling on torus cutters. Int J Mach Mach Mater 1(2):166
2. Segonds S, Landon Y, Monies F, Lagarrigue P (2006) Method for rapid characterisation of cutting forces in end milling considering runout. Int J Mach Mach Mater 1(1):45–61
3. Gilles P, Monies F, Rubio W (2007) Optimum orientation of a torus milling cutter: method to balance the transversal cutting force. Int J Mach Tools Manuf 47(15):2263–2272
4. Wan M, Ming-Sheng L, Zhang W-H, Yang Y (2012) A new ternary-mechanism model for the prediction of cutting forces in flat end milling. Int J Mach Tools Manuf 57:34–45
5. Wan M, Altintas Y (2014) Mechanics and dynamics of thread milling process. Int J Mach Tools Manuf 87:16–26
6. Altintas Y, Ko JH (2006) Chatter stability of plunge milling. CIRP Annals - Manufacturing Technology 55(1):361–364
7. Ko JH, Altintas Y (2007) Time domain model of plunge milling operation. Int J Mach Tools Manuf 47(9):1351–1361
8. Witty M, Bergs T, Alexander S, Cabral G (2012) Cutting tool geometry for plunge milling process optimization for a stainless steel. Procedia CIRP 1:506–511
9. Mohamad A (2008) Industrialisation de procédé : contribution à la maîtrise de l'opération de tréflage ou fraisage vertical-approches analytique et expérimentale. PhD thesis. Arts et Métiers ParisTech
10. Ren JX, Yao CF, Zhang DH, Xue YL, Liang YS (2009) Research on tool path planning method of four-axis high-efficiency slot plunge milling for open blisk. Int J Adv Manuf Technol 45 (1–2):101–109
11. Li Y, Liang SY, Petrof RC, Seth BB (2000) Force modelling for cylindrical plunge cutting. Int J Adv Manuf Technol 16(12):863–870
12. Matthieu R (2007) Optimisation de la programmation des MOCN—application aux machines à structure parallèle. PhD thesis, Ecole Centrale de Nantes, Université de Nantes
13. Koenigsberger F, Sabberwal AJP (1961) An investigation into the cutting force pulsations during milling operations. Int J of Mach Tool Des and Res 1(1–2):15–33
14. Tlusty J, MacNeil P (1975) Dynamics of cutting forces in end milling. Annals CIRP, 21–25
15. Qin X, Zhao J, Liu H, Zhang J, Zhao W, Tian Y, Tom MO, Ni W, Liu Y (2007) Mathematical model and simulation of cutting force in plunge milling process. Trans of Tianjin University 13(4):303–307
16. Zhuang K, Zhang X, Zhang X, Ding H (2012). In: Chun-Yi S, Subhash R, Honghai L (eds) Force prediction in plunge milling of inconel 718. Intelligent Robotics and Applications, number 7507 in Lecture Notes in Computer Science. Springer, Berlin Heidelberg, pp 255–263
17. Damir A, Ng E-G, Elbestawi M (2010) Force prediction and stability analysis of plunge milling of systems with rigid and flexible workpiece. Int J Adv Manuf Technol 54(9–12):853–877
18. Kielbus A (2007) Microstructure and mechanical properties of elektron 21 alloy after heat treatment. J of Achiev in Mater and Manuf Eng 20(92007):127–130
19. Danis I, Wojtowicz N, Monies F, Lamesle P, Lagarrigue P (2013) Cutting conditions and surface integrity during dry plunge-milling of a wrought magnesium alloy. Procedia Eng 63:36–44
20. Danis I, Wojtowicz N, Monies F, Lagarrigue P (2014) Influence of dry plunge milling conditions on surface integrity of magnesium alloys. Int J of Mechatronics and Manuf Syst 7(2–3):141–156
21. Kielbus A (2007) Corrosion resistance of elektron 21 magnesium alloy. J of Achiev in Mater and Manuf Eng 22(1):29–32
22. Lyon P, Syed I, Heaney S (2007) Elektron 21—an aerospace magnesium alloy for sand cast and investment cast applications. Adv. Eng. Mater. 9(9):793–798
23. Germain D (2011) Development of a predictive force model integrating the contact on the clearance face: application to superfinish turning of copper Cu-c2. PhD thesis, Arts et Métiers ParisTech
24. Merchant ME (1945) Mechanics of the metal cutting process. i. orthogonal cutting and a type 2 chip. J Appl Phys 16(5): 267
25. Merchant ME (1945) Mechanics of the metal cutting process. II. plasticity conditions in orthogonal cutting. J Appl Phys 16 (6):318
26. Albrecht P (1960) New developments in the theory of the metal-cutting process: Part I. The ploughing process in metal cutting. J Eng Ind 82(4):348–357
27. Fang N (2005) Tool-chip friction in machining with a large negative rake angle tool. Wear 258(5–6):890–897